INL/EXT-16-39965 Rev. 1

September 2016

UO_2 Grain Growth: Developing Phase Field Models for Pore Dragging, Solute Dragging and Anisotropic Grain Boundary Energies

K. Ahmed
M. Tonks
Y. Zhang
B. Biner

INL/EXT-16-39965 Rev. 0

UO_2 Grain Growth: Developing Phase Field Models for Pore Dragging, Solute Dragging and Anisotropic Grain Boundary Energies

K. Ahmed
M. Tonks[*]
Y. Zhang
B. Biner

September 2016

Idaho National Laboratory
Fuel Modeling and Simulation Department
Idaho Falls, Idaho 83415

[*]**Pennsylvania State University**
Department of Mechanical and Nuclear Engineering
State College, PA

Prepared for the
U.S. Department of Energy
Office of Nuclear Energy
Under U.S. Department of Energy-Idaho Operations Office
Contract DE-AC07-99ID13727

ABSTRACT

A detailed phase field model for the effect of pore drag on grain growth kinetics was implemented in MARMOT. The model takes into consideration both the curvature-driven grain boundary motion and pore migration by surface diffusion. As such, the model accounts for the interaction between pore and grain boundary kinetics, which tends to retard the grain growth process. Our 2D and 3D simulations demonstrate that the model capture all possible pore-grain boundary interactions proposed in theoretical models. For high enough surface mobility, the pores move along with the migrating boundary as a quasi-rigid-body, albeit hindering its migration rate compared to the pore-free case. For less mobile pores, the migrating boundary can separate from the pores. For the pore-controlled grain growth kinetics, the model predicts a strong dependence of the growth rate on the number of pores, pore size, and surface diffusivity in agreement with theroretical models. An evolution equation for the grain size that includes these parameters was derived and showed to agree well with numerical solution. It shows a smooth transition from boundary-controlled kinetics to pore-controlled kinetics as the surface diffusivity decreases or the number of pores or their size increases. This equation can be utilized in BISON to give accurate estimate for the grain size evolution. This will be accomplished in the near future. The effect of solute drag and anisotropy of grain boundary on grain growth will be investigated in future studies.

Table of Contents

1. Introduction

All physical properties of polycrystalline solids such as yield stress, fracture strength, electrical breakdown strength, dielectric constant, etc. are strongly dependent on the grain size [1, 6]. This is due to the prominent role of grain boundaries in influencing material properties. Samples with smaller grain size have higher grain boundary area per unit volume. Furthermore, it was found out that the performance of several materials under extreme conditions, such as irradiation, high temperature, high stresses, etc., is highly affected by the grain size [1, 7]. For instance, theory and experiments showed a significant reduction of fission-gas release and dimensional changes in UO_2 fuel with increasing grain size [7]. Therefore, investigating the kinetics of grain growth in uranium dioxide, UO_2, is important for understanding the performance of the main nuclear fuel in nuclear reactors. Pore drag, solute drag and anisotropy of grain boundary energy may affect the overall grain growth rates in materials [1]. Here we focus our attention on the effect of pore drag on the process of grain growth.

Grain growth in porous polycrystalline materials, such as UO_2 is a complex process [1-5]. It is well established that the kinetics of grain growth in such materials is strongly influenced by the interaction between pores and grain boundaries [1-5, 8-13]. The pores exert a drag force on the grain boundary and hence hinder the grain boundary migration to the extent that grain growth can completely cease. Nevertheless, when diffusion mechanisms are active, i.e., at high temperature, the pores migrate along with the grain boundaries and the process of grain growth proceeds. However, the presence of pores, whether mobile or immobile, significantly retards grain growth in porous materials relative to the fully dense counterpart [1-5, 8-13].

While a few phase field models of grain growth have been implemented in MARMOT, a model that accounts for the effect of mobile pores on the grain growth kinetics was lacking. Here, we introduce the development of such model and its implementation in MARMOT. The model is shown to capture all possible pore-grain boundary interactions. Mobile pores move as a quasi-rigid-body with a migrating boundary. The grain boundary may separate from less mobile pores. An evolution equation for the grain size that reflects the pore drag effect was derived. It predicts a smooth transition from boundary-controlled to pore-controlled kinetics as the pore mobility decreases or the pore size increases. The dependence of the grain growth/shrinkage rate on the pore size, mobility and shape captured from our simulations agree well with predictions from theoretical models. It also demonstrated that a migrating boundary easily separate from spherical pores, while hardly separate from cylindrical pores. The evolution equation for the grain size derived here will be used in BISON models wherever grain size calculations are required. The effect of solute drag and anistropic grain boundary energy on the grain growth will be investigated later.

2. Theoretical models of particle-grain boundary interactions

In order to investigate the so-called particle-inhibited grain growth, a few theoretical models were proposed in literature [1-5, 8-13]. These models can be classified into two categories depending on whether the particles are treated as mobile or immobile. Second-phase particles such as inclusions or precipitates are usually considered immobile, while pores and bubbles are often considered mobile [1-5, 8-13].

2.1 Immobile particles

The effect of immobile particles on the grain growth process was first studied by Zener [1]. He considered the particles to be immobile, spherical, mono-size, insoluble, and randomly

distributed in the polycrystalline solid. Zener considered the curvature to be the driving force for the boundary motion. The presence of the particles exerts a drag force on the boundary that hinders its motion. The velocity of the boundary is then given

$$v_{\mathrm{b}} = M_{\mathrm{b}}(F_{\mathrm{b}} - N_{\mathrm{p}}F_{\mathrm{p}}), \tag{1}$$

In the above, the subscript b denotes the boundary; v is the grain boundary velocity, M is its mobility, F is its intrinsic (particle-free) driving force, N_{p} is the number of particles per grain boundary area, and F_{p} is the darg force exerted by the particle on the boundary. In the absence of the particles, the intrinsic driving force of the boundary due to its curvature is

$$F_{\mathrm{b}} = \frac{\alpha\gamma_{\mathrm{b}}}{R}. \tag{2}$$

Here, α is a geometric factor that equals 2 for a spherical grain, γ_{b} is the grain boundary energy, and R is the grain radius. The particle drag force depends on the particle shape [14]. For a spherical particle, it is given by

$$F_{\mathrm{p}} = 2\pi r\gamma_{\mathrm{b}}\cos\theta\sin\theta, \tag{3}$$

where r is the particle radius, and θ is the drag angle. For a cylindrical particle, the drag force per unit length of the boundary is

$$F_{\mathrm{p}} = 2\gamma_{\mathrm{b}}\sin\theta, \tag{4}$$

According to Eq. (1), there are two possible scenarios for the interaction between an immobile particle and a grain boundary. First, the boundary can break away and leave the particle behind if $F_{\mathrm{b}} \gg N_{\mathrm{p}}F_{\mathrm{p}}$. Second, the particle can completely pin the boundary and stop the garin growth if $F_{\mathrm{b}} = N_{\mathrm{p}}F_{\mathrm{p}}$.

2.2 Mobile particles

The effect of mobile particles such as pores on the kinetics of grain growth is more complicated. The pores can easily be dragged along by the moving grain boundary [1-5] if one or more of the matter transport mechanisms such as evaporation and condensation, surface diffusion, and lattice (volume) diffusion is active. The first models to investigate the effect of pores on grain growth were proposed by Nichols [3], Brook [4], and carpay [5]. In these simplified models, the microstructure is assumed to be homogeneous. Hence, only one pore-boundary complex is used to represent the behavior of the whole system. Moreover, these models assume the grain and pore to be spherical for the sake of simplicity. Furthermore, these models assume the pore moves as a rigid body without changing shape.

According to these models, there are two different scenarios for the interaction between the pore and the boundary. In one case, the migrating boundary could separate from the pore. In the other, the migrating boundary could drag the pore along with it. If the boundary separates from the pore, the boundary moves with its intrinsic velocity as in the pore-free case.

Pore breakaway will simply occur whenever the grain boundary velocity, v_b exceeds the pore velocity, v_p. This condition can be expressed as [1-5],

$$M_{\mathrm{p}}F_{\mathrm{p}} < M_{\mathrm{b}}(F_{\mathrm{b}} - N_{\mathrm{p}}F_{\mathrm{p}})\,. \tag{5}$$

In the above, the subscript b denotes the boundary and p the pore; N_{p} is now the number of pores per grain boundary area. The forces have the same expressions as in Eqs. (2-4). Rearranging Eq. (5), the pore separation (breakaway) condition is expressed as,

$$F_{\mathrm{b}} > N_{\mathrm{p}}F_{\mathrm{p}} + \frac{M_{\mathrm{p}}F_{\mathrm{p}}}{M_{\mathrm{b}}}\,. \tag{6}$$

On the other hand, if the pore moves along with the boundary, the velocity of the pore-boundary complex (v) can be obtained, by rearranging Eq. (5) and noting that $F_{\mathrm{p}} = v / M_{\mathrm{p}}$, as [1-5]

$$v = M^{\mathrm{eff}} F_{\mathrm{b}}, \tag{7a}$$

$$M^{\mathrm{eff}} = \frac{M_{\mathrm{p}} M_{\mathrm{b}}}{M_{\mathrm{p}} + N_{\mathrm{p}} M_{\mathrm{b}}}. \tag{7b}$$

In the above, M^{eff} is the effective mobility of the pore-boundary complex. Two limiting cases are immediately obtained from Eq. (7). When $M_{\mathrm{p}} \gg N_{\mathrm{p}} M_{\mathrm{b}}$, the effective velocity of the pore-boundary complex reduces to $v = M_{\mathrm{b}} F_{\mathrm{b}}$, hence the effect of pores on the boundary velocity is negligible, a case which is commonly referred to as *boundary-controlled* grain growth. The other limiting case is when $M_{\mathrm{p}} \ll N_{\mathrm{p}} M_{\mathrm{b}}$. In this case, the velocity of the pore-boundary complex becomes $v = M_p F_b / N_p$, and hence the boundary velocity is limited by the pore mobility. This case is referred to as *pore-controlled* grain growth. Under several assumptios on the pore and boundary shapes and nature of motion, expressions for the pore mobility for different transport mechanisms were derived [1-5].

In the classical homogeneous models summarized above, it was assumed that the microstructure is homogeneous, and the details of the pore and boundary shapes and nature of motion were neglected. In order to alleviate these shortcomings, more advanced models were proposed [8-13, 15-18]. The first are of the so-called sharp-interface models [8-13]. In that description, the grain boundary moves by mean curvature while the pore migrates via surface diffusion. Surface diffusion is expected to be the dominant mechanism of pore migration in

solids at temperatures of interest [1]. Moreover, the shrinkage of pores is ignored and hence the pores have a prescribed constant volume.

The mathematical formulation of the sharp-interface dynamics of the co-evolution of pores and grain boundary can be summarized as follows. The grain boundary moves under the influence of its curvature according to the relation,

$$v_b = -\gamma_{\mathrm{b}} M_b \kappa_b \,. \tag{8}$$

Here, v_{b} is the velocity of a grain boundary element, γ_{b} is the grain boundary energy, M_{b} is the grain boundary mobility, and κ_{b} is the grain boundary local curvature (mean curvature in 3D). The curvature is positive for convex surfaces and negative for concave surfaces. On the other hand, the pore moves via surface diffusion as

$$v_{\mathrm{p}} = \frac{\gamma_{\mathrm{s}} D_{\mathrm{s}} \delta_{\mathrm{s}} \Omega}{k_B T} \nabla_{\mathrm{s}}^2 \kappa_{\mathrm{s}} \,. \tag{9}$$

In Eq. (9), v_p is the velocity of a surface element of the pores, γ_{s} is the pore (free) surface energy, D_{s} is the surface diffusivity, δ_{s} is the surface layer width, Ω is the atomic volume, k_B is the Boltzmann's constant and T is the absolute temperature, ∇_s^2 is the surface Laplacian (Laplace operator on the surface), and κ_s is the curvature of the pore (free) surface

By solving Eq. (8) and Eq. (9) simultaneously, the co-evolution of pores and grain boundaries in a porous polycrystalline solid can be tracked. In order to solve these equations, boundary conditions at the pore tip must be supplemented. The appropriate boundary conditions are the continuity of the chemical potential and surface flux. From Eq. (8) and Eq. (9), this translates into the continuity of κ_{s} and $\nabla \kappa_{\mathrm{s}}$ at the pore tip. Moreover, mechanical equilibrium

requires that the tension forces to be balanced at the pore tip. This means that the equilibrium dihedral angle, Ψ defined by $\Psi = 2\cos^{-1}(\gamma_{gb} / 2\gamma_s)$ must be maintained during the evolution.

Solving such models for general pore and boundary shapes are extremely difficult [8-13]. In fact in most cases only 2D solutions for idealized geometries were obtained. This has motivated us to introduce a phase field (diffuse-interface) description of the problem. Phase field models can easily handle general pore and boundary morphologies since tracking the interface is not required in such models.

3. Phase field model of pore-grain boundary interactions

3.1 Model description

The model can be summarized as follows. A combination of conserved and non-conserved order parameters (phase fields) is used to fully represent the microstructure of a porous polycrystalline solid [15-18]. The conserved field, $c(x,t)$, represents the vacancy site fraction, and it takes the value of 1 in the pore phase and 0 in the solid phase. In order to distinguish between different grains with different orientations in the solid phase, a set of non-conserved order parameters, η_α, are used, where $\alpha = 1,2,....p$, with p being the total number of grains with different orientations in the solid. $\eta_\alpha = 1$ in the α-th grain and 0 otherwise

The free energy of the heterogeneous system of pores and grains can be constructed as follows [18]

$$F = \int f(c,\eta_1,...,\eta_p) + \frac{1}{2}\kappa_c \left|\nabla c\right|^2 + \frac{1}{2}\sum_{\alpha=1}^{p} \kappa_\eta \left|\nabla \eta_\alpha\right|^2 \quad d^3r \,. \tag{10}$$

In the above expression, the first term represents the bulk free energy density. The two gradient terms account for the excess free energy due to pore (free) surfaces and grain boundaries,

respectively. The bulk free energy density used here is simply a positive-definite multi-well potential that represents the equilibrium phases. It has the form [15-18],

$$f(c,\eta_1,...,\eta_p) = Ac^2(1-c)^2 + B\left[(1-c)^2 + 6\,c\sum_\alpha \eta_\alpha^2 - 4(1+c)\sum_\alpha \eta_\alpha^3 + 3(\sum_\alpha \eta_\alpha^2)^2\right]. \quad (11)$$

This particular from has (p+1) minima that correspond to the pore phase and all grains in the solid phase. A, B, κ_ρ and κ_η are material constants related to surface and grain boundary eneries.

The conserved density field evolves according to a Cahn-Hilliard equation [19] in the form,

$$\mu = \partial f(c,\eta_1,....,\eta_\alpha,....,\eta_p)/\partial c - \kappa_c \nabla^2 c\,, \quad (12a)$$

$$\frac{\partial c}{\partial t} = \nabla \cdot M \nabla \mu\,. \quad (12b)$$

Here, M is the mobility and μ is the chemical potential. We assume that surface diffusion is the dominant mechanism for pore migration since it usually the case for most solids. This also allows us to directly compare our results with the classical and sharp-interface models discussed above. In order to simulate surface diffusion, we use the following form for the mobility

$$M = 630\,M_0 c^4(1-c)^4\,, \quad (13)$$

which is non-zero only at the free surface. M_0 is a material property directly related to the surface diffusivity [18].

The non-conserved order parameters are governed by Allen-Cahn equations [20] as

$$\frac{\partial \eta_\alpha}{\partial t} = -L\,\delta F/\delta \eta_\alpha = -L\,[\partial f(c,\eta_1,....,\eta_\alpha,....,\eta_p)/\partial \eta_\alpha - \kappa_\eta \nabla^2 \eta_\alpha] \quad \forall \alpha, \alpha = 1, 2....p\,. \quad (14)$$

Here, L, the Allen-Cahn mobility, is a material property that is related to the grain boundary mobility [17]. Using constant gradient and mobility coefficients is equivalent to the assumption of isotropic grain boundary energy and mobility.

The phase field model parameters are directly related to the thermodynamic and kinetic parameters that appear in the sharp-interface models (Eqs. 8 and 9). Such relation can be established using formal asymptotic analysis as was conducted in [18]. This analysis demonstrates that the phase field model recovers the sharp-interface counterpart. From that analysis the model parameters are determined as

$$A = \frac{12\gamma_{\mathrm{s}} - 7\gamma_{\mathrm{b}}}{\ell}, \tag{15a}$$

$$B = \frac{\gamma_{\mathrm{gb}}}{\ell}, \tag{15b}$$

$$\kappa_\eta = \frac{3}{4}\gamma_{\mathrm{b}}\,\ell, \tag{15c}$$

$$\kappa_c = \frac{3}{4}\ell(2\gamma_{\mathrm{s}} - \gamma_{\mathrm{b}}), \tag{15d}$$

$$L\kappa_\eta = \gamma_{\mathrm{b}} M_b, \tag{15e}$$

$$M_0(\kappa_c + \kappa_\eta) = \frac{\gamma_{\mathrm{s}} D_{\mathrm{s}} \delta_{\mathrm{s}}\, \Omega}{k_B T}. \tag{15f}$$

In the above, ℓ is the diffuse interface width. These relations fix all the model parameters in terms of physical material properties, which facilitates obtaining quantitative results that can be compared theory and experiments.

3.2 Model implementation in MARMOT

A fully-coupled, fully-implicit finite-element scheme was used to solve the phase field kinetic equations. This scheme was implemented in MARMOT [21]. First, the varitional (weak) form of the partial differential equations (PDEs) (see Eqs (12) and (14)) was obtained in a regular manner. Specifically, the residual equations in the weak form are

$$(\mu,\phi)-(\partial f/\partial c,\phi)-(\kappa_c\nabla c,\nabla\phi)+<\kappa_c\nabla c\cdot\mathbf{n},\phi>=0\,, \tag{16a}$$

$$(\partial c/\partial t,\phi)+(M\nabla\mu,\nabla\phi)-<M\nabla\mu\cdot\mathbf{n},\phi>=0\,, \tag{16b}$$

$$(\partial\eta_\alpha/\partial t,\phi)+L(\partial f/\partial\eta_\alpha,\phi)+L(\kappa_\eta\nabla\eta_\alpha,\nabla\phi)-L<\kappa_\eta\nabla\eta_\alpha\cdot\mathbf{n},\phi>=0\quad\forall\alpha,\alpha=1,2....p\,. \tag{16c}$$

In the above ϕ is a test function, $(\cdot,\cdot)$ stands for interior integration, and $<\cdot,\cdot>$ for boundary integration. Linear Lagrange discretization of Eqs (16a-16c) employing four-node quadrilateral elements in 2D and eight-node hexahedral elements in 3D was performed. The time integration was carried out via a second-order Backward Differentiation Formula (BDF2). The nonlinear system was solved using the Jacobian-Free Newton Krylov (JFNK) method [22]. In all simulations, the interface was resolved by at leat six elements. Adaptive mesh size and time step were utilized to reduce the computational time. On averge, 2D simulatios took from few hours to few days on 24 cores, while 3D simulations took between few days to few weeks on 216 cores.

4. Results and discussion

The main goal of the investigation presented here is to quantify the effect of pore drag on the grain growth kinetics. A specific set of parametrs representing a particular material cannot be used to account for all possible pore-grain boundary interactions. Therefore, without loss of generality, we use the following normalized model parameters: $A=4.25$, $B=0.25$, $\kappa_\eta=3.0$,

$\kappa_c = 9.0$, $L = 1.0$. These parameters give a normalized grain boundary energy, e.g., $\gamma_b = 1.0$, a normalized surface energy, $\gamma_s = 2.0$, and a normalized interface width, $\ell = 4.0$. The pore radius and surface diffusivity (and hence M_0) were varied to study the different scenarios of por-grain boundary interactions. Moreover, to facilitate comparison with theory, we choose a few idealized 2D and 3D pore and grain boundaries shapes.

4.1 Shrinkage of an isolated circular grain with boundary pores

Our first case study is the shrinkage of an isolated circular grain emedded in a large matrix grain. The domain size was 912×912 and the initial circular grain radius was 300. Periodic boundary conditions were applied in both directions. The pore radius and surface mobility were varied to investigate all possible pore-boundary interactions.

For the case of pore-free grain shrinkage, the boundary velocity is inversely proportional to its radius as given by Eq. (8). This gives rise to the well-known parabolic law, which has the form [1]:

$$R^2(t) - R^2(0) = -k\,t\,, \tag{17a}$$

$$k = 2\gamma_b M_b = 2L\kappa_\eta\,. \tag{17b}$$

Here, $R(t)$ is the grain radius at time t, $R(0)$ is the initial grain radius, and k is the rate constant. On the other hand, in the presence of pores, the boundary velocity is given by Eq. (7) as discussed before. For the current 2D (cylindrical) pore and boundary shapes, $F_b = -\gamma_b / R$, $N_p = n_p / 2\pi R L_{cyl}$, where n_p is the number of pores on the boundary and L_{cyl} is the length of the cylindrical grain. Moreover, if one ignores coarsening and densification and assume the pore moves along with the boundary as a rigid body, the pore radius r remains constant and the pore mobility can be derived as [1-5, 8-13]

$$M_{\mathrm{p}} = \frac{D_{\mathrm{s}}\delta_{\mathrm{s}}\,\Omega}{\pi k_B T r^3 L_{\mathrm{cyl}}}\,. \tag{18}$$

Hence, if one assumes $v = dR/dt$, Eq. (7) can be directly integrated and the final form is

$$\frac{n_{\mathrm{p}} M_{\mathrm{b}}}{2\pi L_{\mathrm{cyl}}}[R(t) - R(0)] + \frac{M_{\mathrm{p}}}{2}[R^2(t) - R^2(0)] = -\gamma_{\mathrm{b}} M_{\mathrm{b}} M_{\mathrm{p}}\, t\,, \tag{19}$$

Clearly, two limiting cases may arise. For the boundary-controlled shrinkage $(M_{\mathrm{p}} \gg n_{\mathrm{p}} M_{\mathrm{b}} / \pi L_{\mathrm{cyl}})$, the shrinkage kinetics follows Eq. (17) as in the pore-free case. On the other hand, for the pore-controlled kinetics $(M_{\mathrm{p}} \ll n_{\mathrm{p}} M_{\mathrm{b}} / \pi L_{\mathrm{cyl}})$, the shrinkage kinetics follows

$$R(t) - R(0) = -k\,t\,, \tag{20a}$$

$$k = 2\pi\gamma_{\mathrm{b}} M_{\mathrm{p}} L_{\mathrm{cyl}} / n_{\mathrm{p}} = \frac{2M_0(\gamma_{\mathrm{b}}/\gamma_{\mathrm{s}})(\kappa_\eta + \kappa_c)}{n_{\mathrm{p}} r^3}\,. \tag{20b}$$

In the second equation, we used Eq. (18) and (15f) to arrive at the second equality that expresses the rate constant in terms of the phase field model parameters.

All the scenarios discussed above were investigated in our simulations. For the pore-free case, the kinetics followed Eq. (17). The rate constant was calculated to be 5.9, which is very close to the exact value of 6.0 expected from Eq. (17.b).

In order to account for the effect of pore drag on the kinetics, 8 pores were evenly distributed on the boundar as shown in Fig. 1. The quasi-static rigid-body motion of the pores with the boundary, which is usually assumed in the theoretical models, is evident from the figure. The effect of the surface diffusivity on the kinetics is captured in Fig. 2. The shrinkage kinetics changes from boundary-controlled to pore-controlled as the surface mobility (diffusivity) decreases. For very high surface mobility (see Fig. 2(a)), the kinetics is boundary-controlled and follows the parabolic law of Eq. (17). On the other hand, for low surface mobilities, the kinetics

is pore-controlled and follows the linear law in Eq. (20) as shown in Fig. 2(b). The rate constant for $M_0 = 4.0$ and $r = 20$ was found to be $k = 5\times10^{-4}$ which is relatively close to the exact value $k = 7.5\times10^{-4}$ calculated from Eq. (20b). k also increases linearly with M_0 , in agreement with Eq. (20b), as captured in Fig 2(b). The effect of the pore radius on the pore-controlled kinetics was also studied. Fig. 3 shows the strong dependence of the rate constant on the pore radius. The dependence agrees wells with Eq. (20b) as captured in Fig. 3.

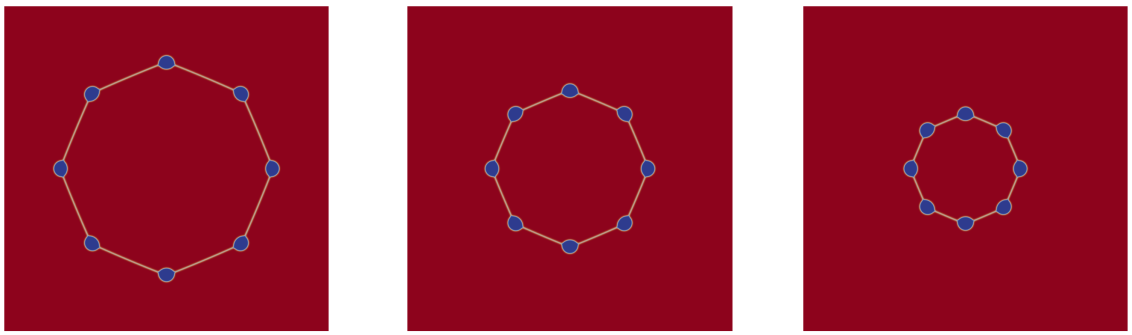

Fig. 1. Snapshots of the shrinkage of an isolated circular grain with boundary pores. The pores take on their equilibrium lenticular shape. For high surface mobility, the pores move along with the boundary as a rigid-body.

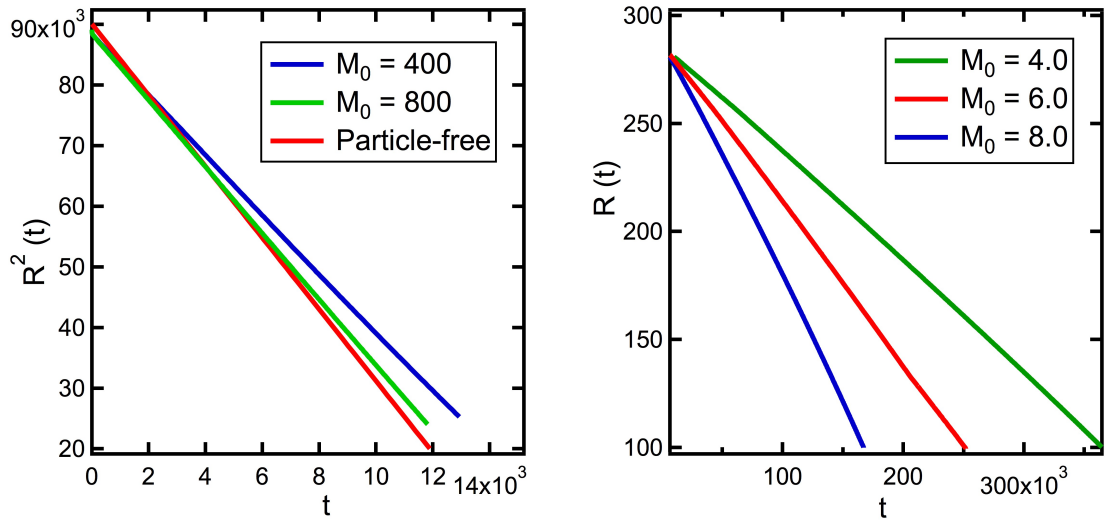

(a) Boundary-controlled kinetics (b) Pore-controlled kinetics

Fig. 2. The dependence of the shrinkage kinetics on the surface mobility. (a) The boundary-controlled kinetics follows the parabolic law given by Eq. (17), (b) the pore-controlled kinetics follows the linear law in Eq. (20). For the pore-controlled kinetics, the rate constant increases linearly with the surface mobility in agreement with Eq. (20.b).

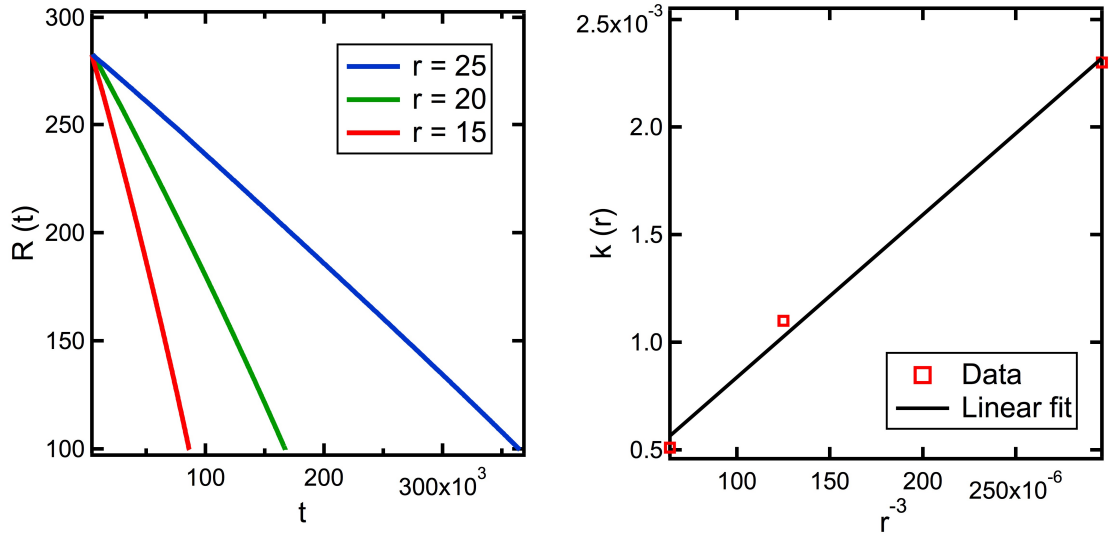

Fig. 3. The dependence of the pore-controlled shrinkage kinetics on the pore radius. The evolution of the grain radius as function of the pore radius is shown in the left figure. The dependence of the rate constant on the pore radius agrees well with Eq. (20.b) as captured in the figure on the right.

4.2 Shrinkage of a four-sided grain with edge and corner pores

According to the well-known topological analysis of grain growth put forward by Neumann and Mullins [1, 23], a grain with more than six sides will grow, while a grain with less than six

sides will shrink. A grain with six sides is static. The growth/shrinkage rate of a grain with n sides is given by

$$\frac{dA(n)}{dt} = \frac{\pi}{3}\gamma_{\mathrm{b}} M_{\mathrm{b}}(n-6), \tag{21}$$

where, $A(n)$ is the area of a grain with n sides. Klinger et. al. have recently generalized the analysis to the case where pores are present on the grain boundary [13]. They have derived an equation for the grain size that has the form

$$\frac{dR}{dt} = \frac{\sqrt{3}\pi M_{\mathrm{b}}\gamma_{\mathrm{b}} M_{\mathrm{p}}(n-6)}{6(\sqrt{3}\pi M_{\mathrm{p}} R + nM_{\mathrm{b}})}. \tag{22}$$

This form indicates that also a grain with more than six sides grows, while one with less than six sides shrinks as in the pore-free case. However, the growth/shrinkage kinetics is now dependent on the pore size and mobility. Again, if one assumes the pore size rmains constant during grain growth/shrinkage, Eq. (22) can be directly integrated to give a formula equivalent to Eq. (19), e.g.,

$$6nM_{\mathrm{b}}[R(t)-R(0)] + 3\sqrt{3}\pi M_{\mathrm{p}}[R^2(t)-R^2(0)] = \sqrt{3}\pi M_{\mathrm{b}}\gamma_{\mathrm{b}} M_{\mathrm{p}}(n-6)t. \tag{23}$$

In the same manner as before, two limititng cases can be identified. For the boundary-controlled shrinkage ($M_{\mathrm{p}} \gg 2nM_{\mathrm{b}}/\sqrt{3}\pi$), the shrinkage kinetics follows the Neumann and Mullins relation (e.g., Eq. (21)) as in the pore-free case. On the other hand, for the pore-controlled kinetics ($M_{\mathrm{p}} \ll 2nM_{\mathrm{b}}/\sqrt{3}\pi$), the shrinkage kinetics follows

$$R(t) - R(0) = -kt, \tag{24a}$$

$$k = (n-6)\pi\gamma_{\mathrm{b}} M_{\mathrm{p}}/2\sqrt{3}n = \frac{(n-6)M_0(\gamma_{\mathrm{b}}/\gamma_{\mathrm{s}})(\kappa_\eta + \kappa_c)}{2\sqrt{3}nr^3}. \tag{24b}$$

In Eq. (24b), Eq. (18) and (15f) were used to relate the rate constant to the phase field model parameters.

We study here the shrinkage of a four-sided grain. The initial grain size of the four-sided grain was 200. In this example, natural boundary conditions for all the variables were applied. For the pore-free case, the area decreased linearly with time, in agrrement with Eq. (21), as shown in Fig. 5(b). The rate constant was found tobe 5.9, which is slightly lower than the exact vakue of 6.28. We then investigate the effect of pores on the shrinkage kinetics. Two different pore configurations were studied, e.eg., edge (two-grain junction) pores and corner (triple junction) pores. Snapshots of the shrinkage of a four-sided grain with edge/corner pores are presented in Fig. 4. Similar to the circular grain case, the pores migrate with the boundary as a qusi-rigid-body. The equilibrium shapes of edge and corner pores are kept during the evolution as evident from the figure. For the case of edge pores with $M_0 = 4.0$ and $r = 20$, the rate constant take on the value $k = 3.3\times10^{-4}$, which is relatively close to the exact value $k = 4.3\times10^{-4}$ calculated from Eq. (24b). For corner pores, the rate constant was $k = 2.8\times10^{-4}$. Therefore, edge pores are more mobile and retard the grain boundary less than corner pores. This prediction is in agreement with the analysis presented in [12].

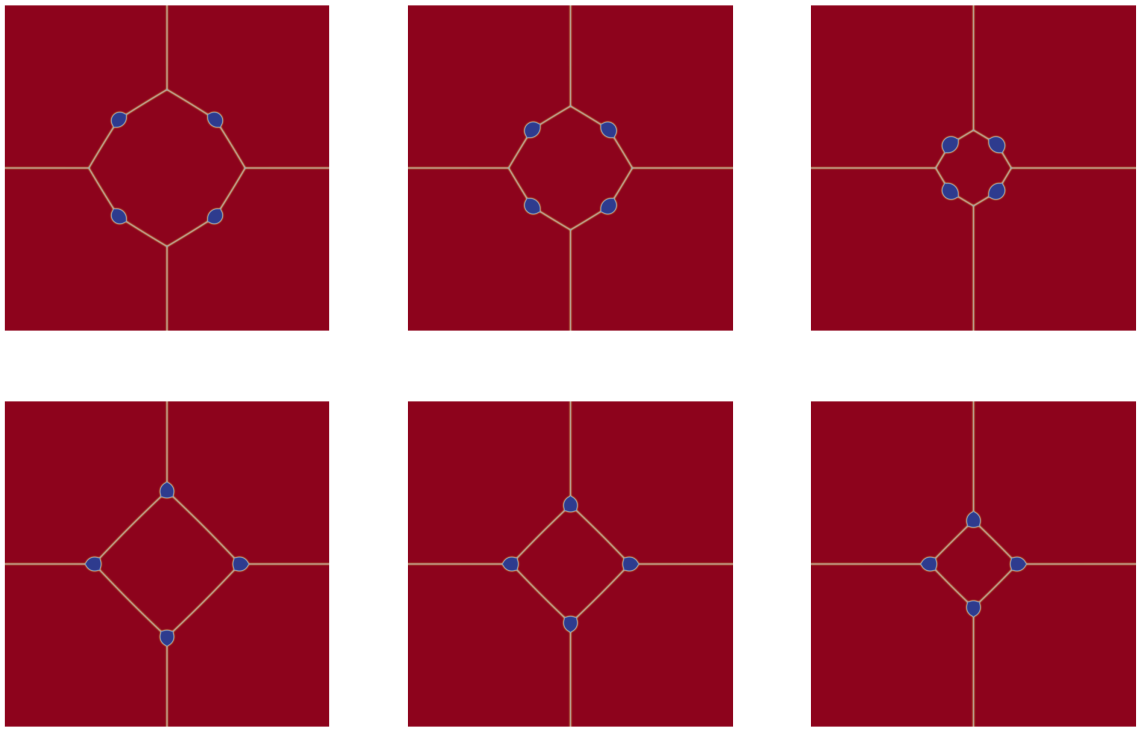

Fig. 4. Snapshots of the shrinkage of a four-sided grain with edge (two-grain junction) pores (upper row) and corner (triple junction) pores (lower row). Similar to Fig. 1, the quasi-static rigid-body motion of the pores with the boundary is evident. Note that the equilibrium shapes of the edge and corner pores are different as expected.

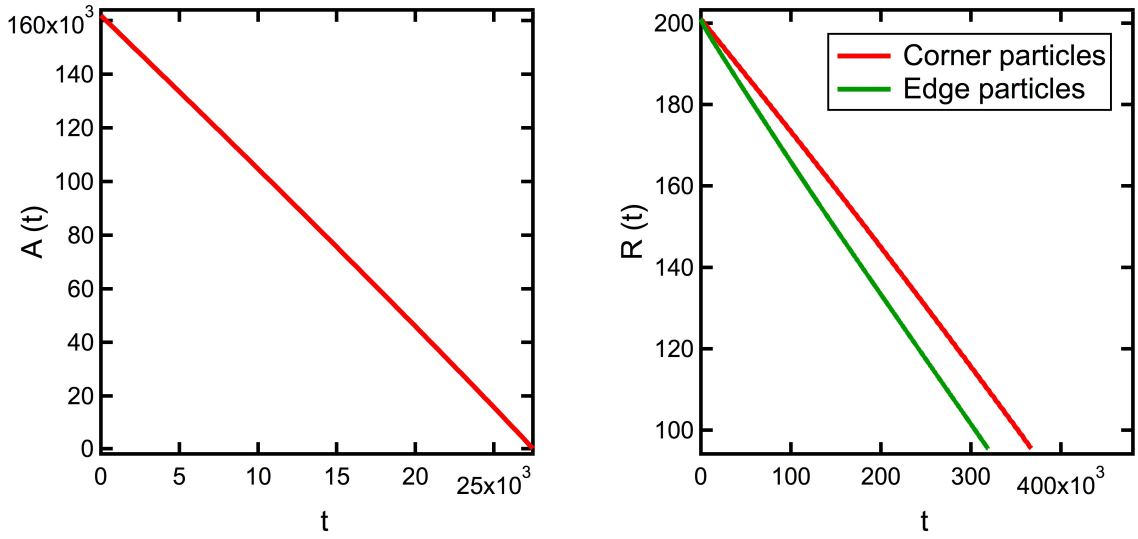

(a) Pore-free shrinkage (b) Pore-controlled shrinkage

Fig. 5. Shrinkage kinetics of a four-sided grain, (a) particle-free case, (b) particle-controlled case with edge/corner particles located on the boundary. The kinetics in (a) and (b) follows closely Eq. (21) and Eq. (24), respectively (see text). Corner pores retards the shrinkage/growth kinetics more than edge pores.

4.3 3D simulations of the shrinkage of a cylindrical grain with spherical boundary pores

Our last case study is devoted for inestigating the shrinkage of a cylindrical grain embedded in a large matrix grain with spherical pores located on its boundary. The nature of drag and motion of 3D spherical particles is completely different from the 2D cylindrical particles discussed above [1-5, 14]. For instance, it is well-known that it is easier for a migrating boundary to break away from a 3D spherical particle than from a 2D (cylindrical) particle. Also the expression for the pore mobility of a spherical particle differs from the one for a cylindrical particle.

Following the same procedure conducted for the shrinking circular grain in section 4.1, one can show that the evolution equation for the cylindrical grain radius is the same as Eq. (19). However, the pore mobility of the 3D spherical pore is now given by (to be compared with Eq. (18)) [1-5]

$$M_{\mathrm{p}} = \frac{D_{\mathrm{s}}\delta_{\mathrm{s}}\Omega}{\pi k_B T r^4}. \tag{25}$$

Again as in the 2D case, for the case of pore-free or boundary controlled kinetics, the shrinkage proceeds according to the parabolic law of Eq. (17). For the case of pore-controlled shrinkage, the grain radius decrease linealy with as in Eq. (20.a), but the rate constant has now the form (compare it with Eq. (20.b))

$$k = 2\pi\gamma_{\mathrm{b}} M_{\mathrm{p}} L_{\mathrm{cyl}} / n_{\mathrm{p}} = \frac{2L_{\mathrm{cyl}} M_0 (\gamma_{\mathrm{b}} / \gamma_{\mathrm{s}})(\kappa_\eta + \kappa_c)}{n_{\mathrm{p}} r^4} \tag{26}$$

In our 3D simulations, the domain size was $500\times500\times160$. The initial cylindrical grain radius was 150 and its height was 160. Periodic boundary conditions were applied in all directions. The pore radius and surface mobility were varied to study their effects on the kinetics. For the pore-free case, the kinetics indeed followed Eq. (17) (see Fig 7(a)). For the pore-controlled case, 16 pores were uniformly distributed on the boundary as shown in Fig. 6. As clear from the figure, the pores move along with the boundary as a rigid-body similar to the 2D case. The kinetics followed Eq. (20.a) with the rate constant now given by Eq. (26). The linear dependence of the rate constant on the surface mobility (see Eq. (26)) is captured in Fig. 7(b). The dependence of the rate constant on the pore size is also cositent with Eq. (26) as obvious from from Fig. 8.

As mentioned above, boundary can separate from 3D spherical particles easier than from 2D cylindrical ones. Therefore, we investigate here the possibility of boundary breakaway. The separation condition is given by Eq. (6). Note that for pore-controlled case, the second term on the right hand side of Eq. (6) can be neglected and the separation condtioin reduces to the same condition for the immobile particle case, e.eg., $F_{\mathrm{b}} > N_{\mathrm{p}} F_{\mathrm{p}}$. For the 3D configuration considered

here and assuming the particle exerts the maximum drag force, e.g., $F_p = \pi r \gamma_b$ (see Eq. (3)), the breakaway condition simply reduces to $2L_{cyl} > n_p r$. We ran multiple 3D simulations with $L_{cyl} = 160$, $n_p = 16$, $M_0 \le 2.0$ and different pore radius for each simulation. Grain boundary separation occurred only when $r < 18$, which is consistent with the separation condition. Snapshots of the separation of the grain boundary from the pores are presented in Fig. 9.

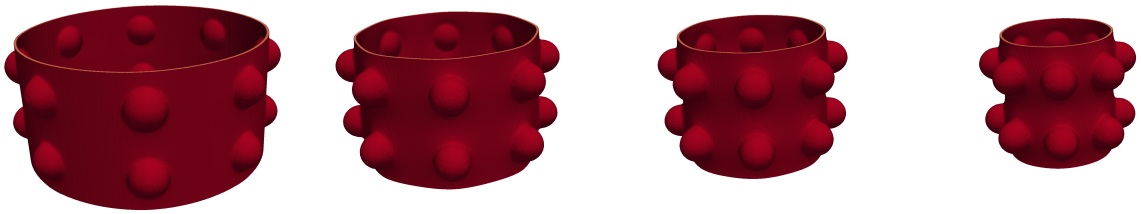

Fig. 6. Snapshots of the shrinkage of a cylindrical circular grain with boundary pores. For high surface mobility, the pores move along with the boundary as a rigid-body.

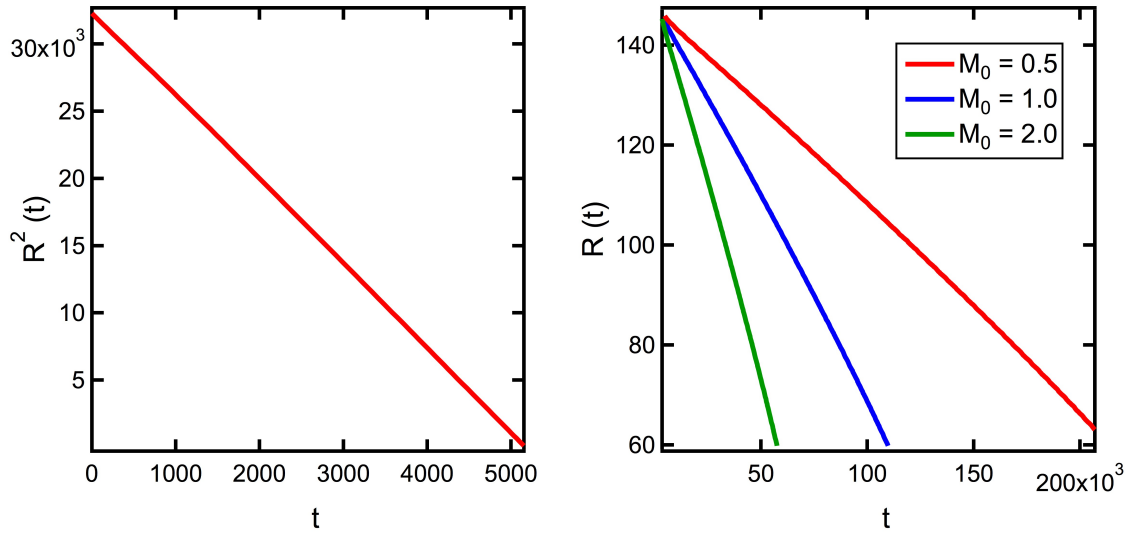

(a) Pore-free kinetics (b) Pore-controlled kinetics

Fig. 7. The shrinkage kinetics of a cylindrical grain with spherical pores on it boundary (see Fig. 6). (a) The pore-free kinetics follows the parabolic law given by Eq. (17), (b) the pore-controlled kinetics follows the linear law in Eq. (20) with the rate constant given by Eq. (26). For the pore-controlled kinetics, the rate constant increases linearly with the surface mobility (M_0) in agreement with Eq. (26).

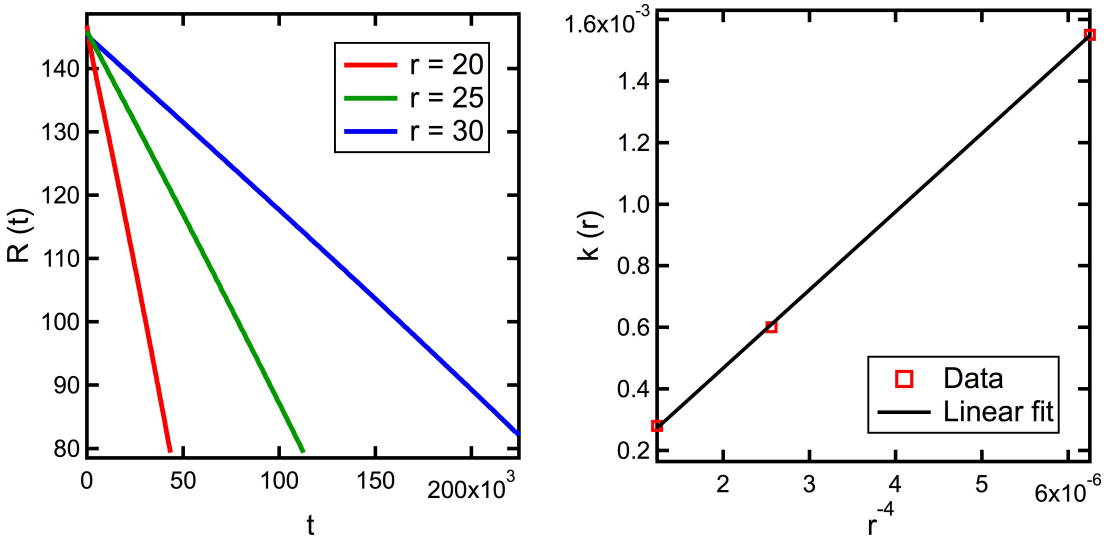

Fig. 8. The dependence of the pore-controlled shrinkage kinetics on the pore radius for the 3D configuration shown in Fig. 6. The evolution of the grain radius as function of the pore radius is shown in the left figure. The dependence of the rate constant on the pore radius agrees well with Eq. (26) as captured in the figure on the right.

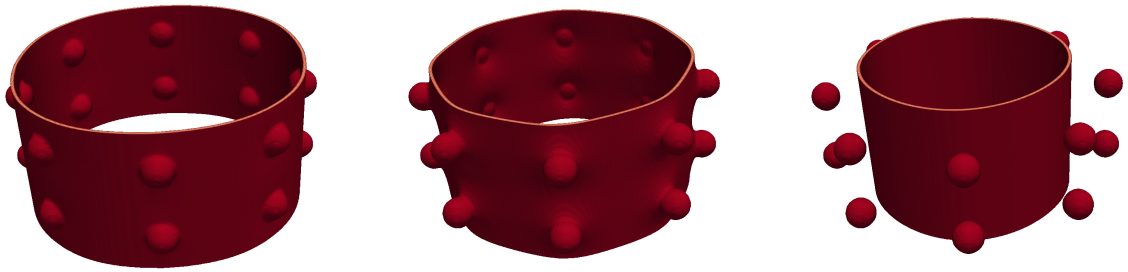

Fig. 9. Snapshots of the sepration of the boundary from the pores. Boundary breakaway took place only when the pore radius was smaller than 18 in agrrement with the separation condition developed in the text.

5. Summary

A quantitative phase field model for the effect of pore drag on the kinetics of grain growth was implemented in MARMOT. The model is able to capture all possible pore-grain boundary interactions. For high surface mobility, the pores can move along with the migrating boundary as a rigid-body. For low surface mobility, the boundary can break away from the pore. An evolution

equation (Eq. (19)) was derived that shows the transition from boundary-controlled kinetics to pore-controlled as the pore mobility decreases or the pore size increases. For the pore-controlled shrinkage/growth, the dependence of the growth/shrinkage rate on the pore mobility and size agrees well with the predicitions from theoretical models. Moreover, it was demonstrated that the pore morphology/configuration also affect the kinetics. Pores on triple junctions retards the grain growth/shrinkage more than pores on two-grain junctions. Furthermore, it was shown that a migrating boundary could easily separate from a 3D spherical particle, while it can hardly break away from a 2D cylindrical particle. While most theoretical models assume idealized pore and grain boundary shapes (e.g., cylindrical and spherical), the phase field model can be applied to general configurations where theoreticl models cannot produce predictive results.

While the investigation conducted here used normalized parameters to study all possible pore-grain boundary interactions, a similar study for uranium dioxide can easily be carried out. This is due to the fact that all the model parameters are directly related to the thermodynamic and kinetic properties. The evolution equations for the grain size that account for pore drag derived here will be used in BISON. This should improve the material and fuel models in BISON that use the grain size as an internal variable. The effects of solute drag and anisotropy of the grain boundary on the kinetics will be considered in future work. Also, while surface diffusion is considered here to be the dominant mechanism of pore migration, evaporation and condensation mechanism may be important for uranium dioxide and will be considered in an upcoming study.

References

[1] Rahaman M N. Ceramic Processing and Sintering. New York: Marcel Dekker; 2003.
[2] Kingery W D, Bowen H K and Uhlmann D R. Introduction to Ceramics. New York: Wiley; 1976.
[3] Nichols FA. J Am Ceram Soc 1968; 51: 468
[4] Brook RJ. J Am Ceram Soc 1969; 52: 56.
[5] Carpay FMA. J Am Ceram Soc 1977; 60: 82.

[6] Armstrong RW. Met Trans 1970; 1: 1169.
[7] Turnbull JA. J Nucl Mater 1974; 50: 62.
[8] Hsueh CH, Evans AG, Coble RL. Acta Metall 1982; 30: 1269.
[9] Spears MA, Evans AG. Acta Metall 1982; 30: 1281.
[10] Svoboda J, Riedel H. Acta Metall Mater 1992; 40: 2829.
[11] Riedel H, Svoboda J. Acta Metall Mater 1993; 41: 1929.
[12] Petrishcheva E, Renner J. Acta Mater 2005; 53: 2793.
[13] Klinger L, Rabkin E, Shvindlerman L, and Gottstein G. J Mater Sci 2008; 43: 5068.
[14] Moelans N, Blanpain B, Wollants P. Acta Mater 2007; 55: 2173.
[15] Tonks, M, Zhang Y, Butterfield A, and Bai XM. Modell Simul Mater Sci Eng 2015; 23, 045009.
[16] Biner B. Modell Simul Mater Sci Eng 2016; 24:035019.
[17] Ahmed K, Yablinsky CA, Schulte A, Allen T, El-Azab A. Modell Simul Mater Sci Eng 2013; 21:065005.
[18] Ahmed K, Allen T, El-Azab A. J Mater Sci 2016; 51: 1261.
[19] Cahn JW. Acta Metall 1961; 9:795.
[20] Allen SM, Cahn JW. Acta Metall 1979;27:1085.
[21] Tonks M, Gaston D, Millett P, Andrs D, Talbot P. Comp Mater Sci 2012; 51: 20.
[22] Knoll D, Keyes D. J Comp Phys 2004; 193: 357.
[23] Mullins W. J Appl Phys 1956; 28: 333.